Science Advances
AAAS

advances.sciencemag.org/cgi/content/full/6/38/eabb0052/DC1

Supplementary Materials for

Intermolecular vibrations mediate ultrafast singlet fission

Hong-Guang Duan, Ajay Jha, Xin Li, Vandana Tiwari, Hanyang Ye, Pabitra K. Nayak, Xiao-Lei Zhu, Zheng Li*, Todd J. Martinez, Michael Thorwart*, R. J. Dwayne Miller*

*Corresponding author. Email: dmiller@lphys.chem.utoronto.ca (R.J.D.M.); michael.thorwart@physik.uni-hamburg.de (M.T.); zheng.li@pku.edu.cn (Z.L.)

Published 18 September 2020, *Sci. Adv.* **6**, eabb0052 (2020)
DOI: 10.1126/sciadv.abb0052

This PDF file includes:

Supplementary Materials

In these Supplementary Materials, we first show the measured X-ray diffraction data of polycrystalline pentacene. Then, we describe the details of the global fitting approach and the obtained two-dimensional (2D) decay-associated map. We further explain the details of the difference of the frequency resolution between the transient grating (TG) and the 2D measurements. In addition, we show the differences of the vibrational frequencies and their Huang-Rhys factors between the singlet excited state and triplet-pair state. Finally, we describe the two-state two-mode model and its parameters. The calculated dynamics along the coupling mode is presented.

I. X-RAY DIFFRACTION DATA

First, we show the measured X-ray diffraction data in Fig. S1.

II. GLOBAL FITTING AND TIMESCALE OF PRIMARY SINGLET FISSION

Multidimensional global fits of both experimental arrays of 2D spectra were performed in accordance with the available algorithm developed earlier (59). A detailed description of the technique can be found in the Supplementary Information of Ref. (60). In this method, a sequence of 2D spectra taken at different T values are collected to form a three-dimensional array S(ω_τ, ω_t, T). This 3D array is then decomposed into a sum of two-dimensional decay-associated spectra $A_i(\omega_\tau, \omega_t)$ with individual exponential decays of correspondingly associated lifetimes τ_i according to

$$S(\omega_\tau, \omega_t, T) = \sum_i A_i(\omega_\tau, \omega_t) \exp(-T/\tau_i). \tag{S1}$$

We apply the global fitting to the 2D spectra of pentacene. The decay-associated spectrum $A_i(\omega_\tau, \omega_t)$ for the retrieved lifetime of 100 fs is shown in Fig. S2. Based on the fitting, we observe one positive peak whose center is located at $(\omega_\tau, \omega_t) = (14600, 14600) cm^{-1}$ and one negative peak at $(\omega_\tau, \omega_t) = (14600, 14000) cm^{-1}$, respectively. Accordingly, a positive peak indicates the decay of magnitude of the center peak which is associated to the GSB. In addition, the negative peak manifests the increase of the amplitude of the ESA process, which shows the generation of the triplet-pair state. Based on our fitting analysis, we observe that the primary step of singlet fission occurs in about 100 fs.

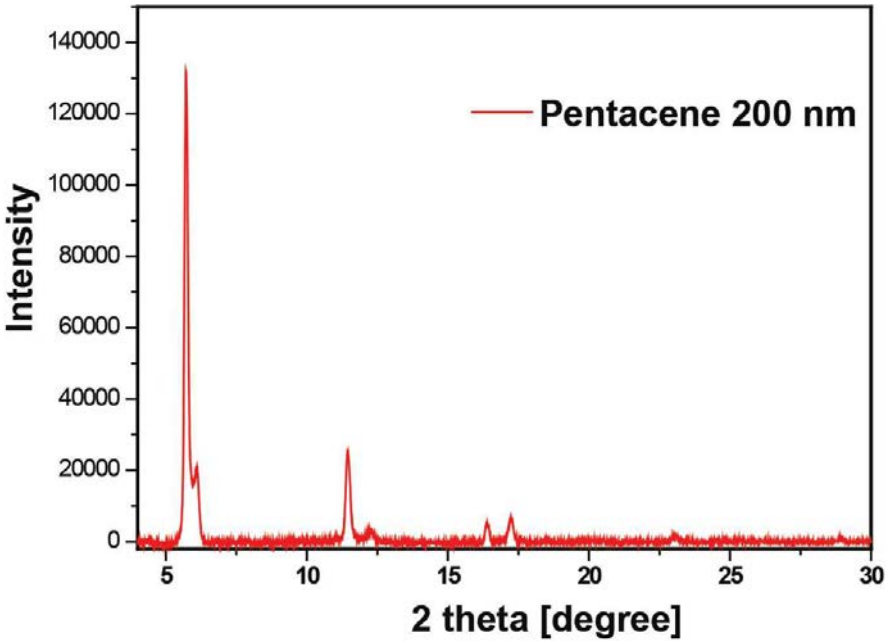

FIG. S1. X-ray diffraction pattern of polycrystalline pentacene.

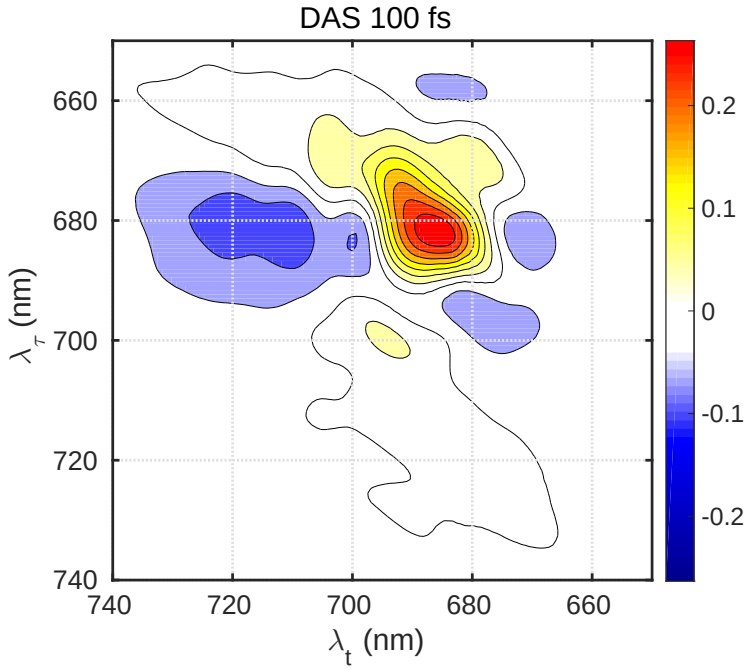

FIG. S2. Retrieved decay-associated spectrum for the lifetime of 100 fs. It shows the generation of the triplet-pair state during the primary step of singlet fission. The red peak indicates that the magnitude of the GSB decreases rapidly and the blue peak manifests the increase of magnitude of the ESA peak.

III. 2D CORRELATION ANALYSIS IN 2D ELECTRONIC SPECTRA

In this brief overview, we summarize the details of the 2D correlation analysis of measured 2D electronic spectra. As described in the previous section, the 2D residuals are obtained after applying the global fitting to the time series of the measured 2D electronic spectra. Then, the correlation analysis can be described by

$$C(\omega_t, \omega_\tau) = \mathrm{corr}\left[R(\omega_t, \omega_\tau, T), R(\omega_\tau, \omega_t, T)\right], \tag{S2}$$

where corr evaluates the correlation with respect to the waiting time T.

IV. FREQUENCY RESOLUTION IN THE TG AND 2D MEASUREMENTS

In this section, we discuss the difference of the frequency resolution in the TG and 2D spectroscopic measurements. In the TG spectrum, we probe the signal up to 2 ps with a time step of 2 fs. Thus, the obtained resolution of the vibrational frequency is $d\omega = 16.5$ cm^{-1}. In our 2D spectroscopic measurement, the 2D spectra are recorded up to 2.1 ps with equally distributed time steps of 10 fs. That is, the frequency resolution is $d\omega = 15.7$ cm^{-1}. This gives rise to a slight difference of the resolved vibrations in TG and 2D spectroscopic measurements.

V. WAVELET TRANSFORM

In this section, we describe the technical principles of the wavelet transform. The details have been presented in Refs. (61, 62). We start from the definition of a zero-mean and short-time oscillating function ψ, called a "mother" wavelet, which is used to decompose a one- or multi-dimensional real signal into different frequency bands. This mother wavelet function is translated in time by t and stretched by the scale of ω^{-1}, giving the wavelet "atom" function

$$\psi_{t,\omega}(t') = \sqrt{\omega}\psi([t' - t]\omega). \tag{S3}$$

It provides the effective basis for the transformation. The two most common transforms are the discrete wavelet transform and the continuous wavelet transform (63). The discrete one decomposes the signal into several frequency bands and is frequently used for data and image compression. The continuous one, which is used in this paper, is based on an expansion of a temporal signal $f(t)$ via the inner product of the function with a wavelet atom,

$$CWT_f(t, \omega) = \int_{-\infty}^{+\infty} dt' f(t')\sqrt{\omega}\psi^*([t' - t]\omega). \tag{S4}$$

The parameter t indicates where the wavelet atom is centered, while the scale parameter ω^{-1} controls the relative width of the wavelet atom compared to the mother wavelet function. This nonlinear integral transform provides a hightime resolution of high-frequency components, while for the slowly varying components of the signal, the frequency resolution is high. It projects the signal onto basis functions with a varying "center" frequency and a varying range fixed by the scaling factor.

VI. QM/MM SIMULATION

The pentacene crystal is modeled as a finite system of the size $76 \times 33 \times 26$Å^3 without periodic boundary condition. The choice of QM and MM regions are illustrated in Fig. S3. The structure of the QM region is optimized while the MM regions remains intact.

VII. CALCULATED VIBRATIONAL MODES AND ASSOCIATED HUANG-RHYS FACTORS

In this section, we present the calculated vibrational modes in the frequency range between 260 and 900 cm^{-1} in Fig. S4.

The calculated vibrational motions of the pronounced high-frequency modes at 1196 and 1517 cm^{-1} are shown in Fig. S5.

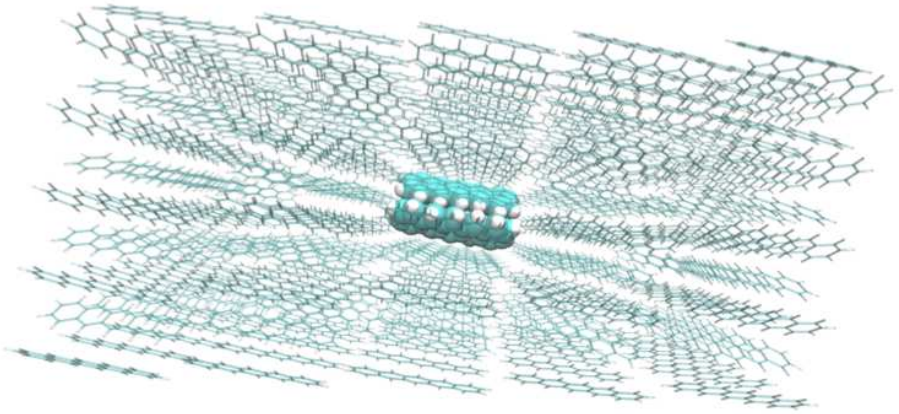

FIG. S3. Illustration of the choice of the QM and MM regions. The atoms in the QM region are depicted as spheres.

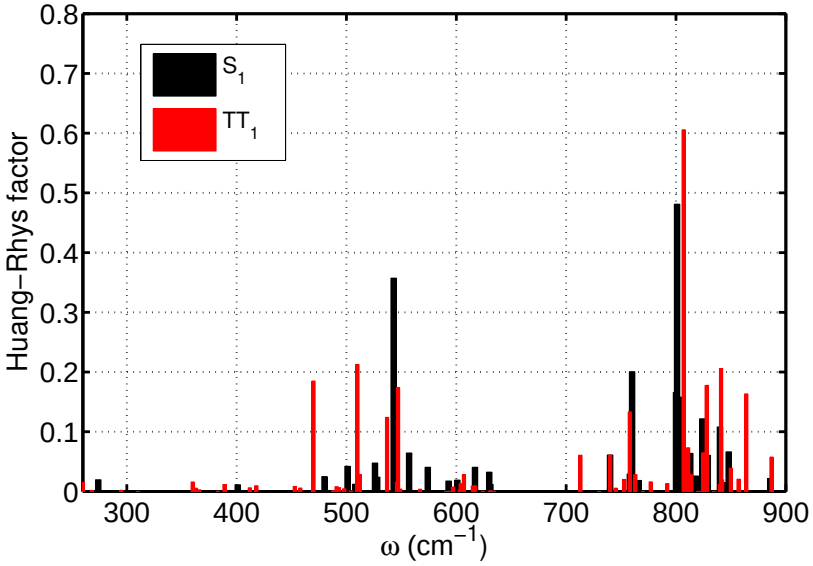

FIG. S4. Calculated vibrational modes in the frequency between 260 cm^{-1} to 900 cm^{-1}.

VIII. CORRELATION ANALYSIS OF LOW-FREQUENCY MODES OF 177 CM^{-1} AND 150 CM^{-1}

In this section, we describe the correlations of the low-frequency modes of 177 cm^{-1} and 150 cm^{-1} on the singlet excited and triplet-pair state, which is calculated from the overlap between the eigenvectors of the vibrational modes in the S_1 and T_1T_1 states. In the TG and 2D spectroscopic measurements, our results strongly suggest that the low-frequency mode of 177 cm^{-1} is coherently transferred to the lower excited state T_1T_1 with the frequency shifted to 150 cm^{-1}. This coherent process has been confirmed by our advanced quantum chemistry calculations. Here, we perform the correlation analysis of the vibrations on both electronic excited states. The results are shown in Fig. S6. Based on the observation, we find a strong magnitude of an off-diagonal peak located at (177 cm^{-1}, 148 cm^{-1}). Clearly, the newly generated mode of 150 cm^{-1} on the T_1T_1 state emerges due to the transfer of the vibrational motion at 177 cm^{-1} and to the change in frequency on the T_1T_1 state.

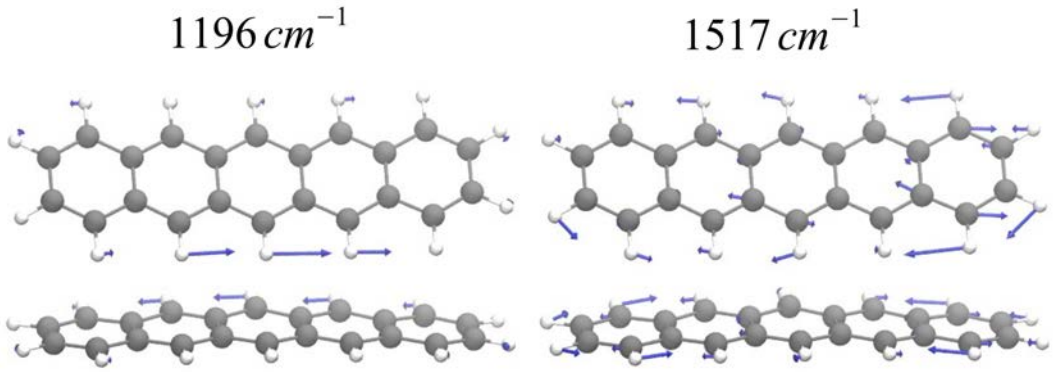

FIG. S5. The calculated vibrational motion of the high-frequency modes at 1196 and 1517 cm^{-1}.

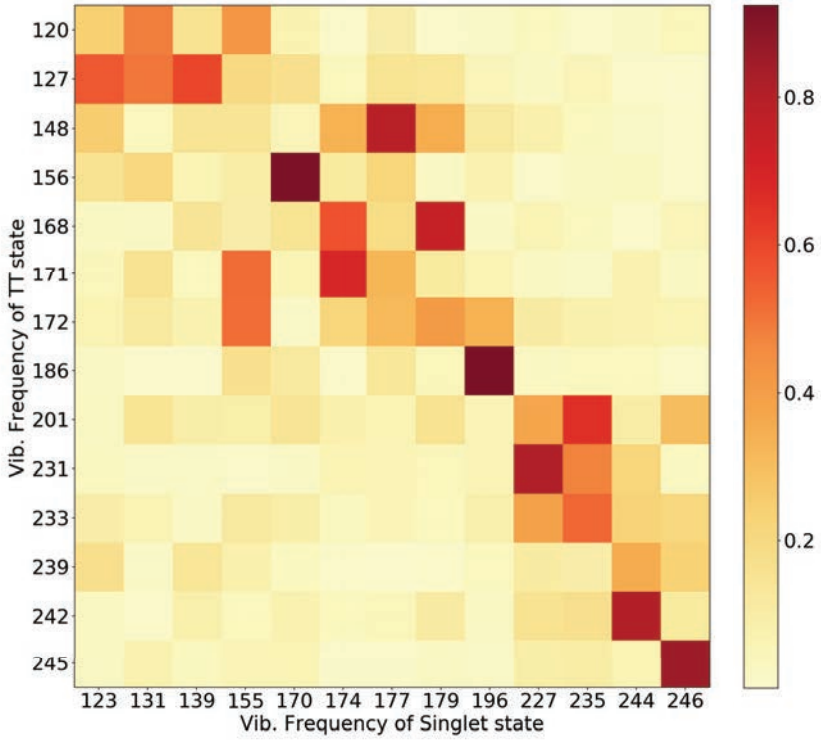

FIG. S6. The correlation analysis of the low-frequency modes in the S_1 and T_1T_1 states. It shows a strong correlation (0.52) between the 177 cm^{-1} mode in the S_1 state and the 148 cm^{-1} mode in the triplet-pair state. The frequencies listed on the axes are not evenly spaced.

IX. CHANGE OF THE ELECTRONIC COUPLING BY INTERMOLECULAR ROCKING MODE

To assign the origin of the intermolecular rocking mode, we examine the change of the electronic coupling between the electronic singlet excited state S_1 and the triple-pair state T_1T_1 by modulating the displacement of rocking motion of pentacene. Based on the calculation in Fig. S7, the electronic coupling between S_1 and T_1T_1 is dramatically

modulated by intermolecular rocking mode. For this reason, we consider this mode as the coupling mode between the singlet and the triplet-pair states in our model.

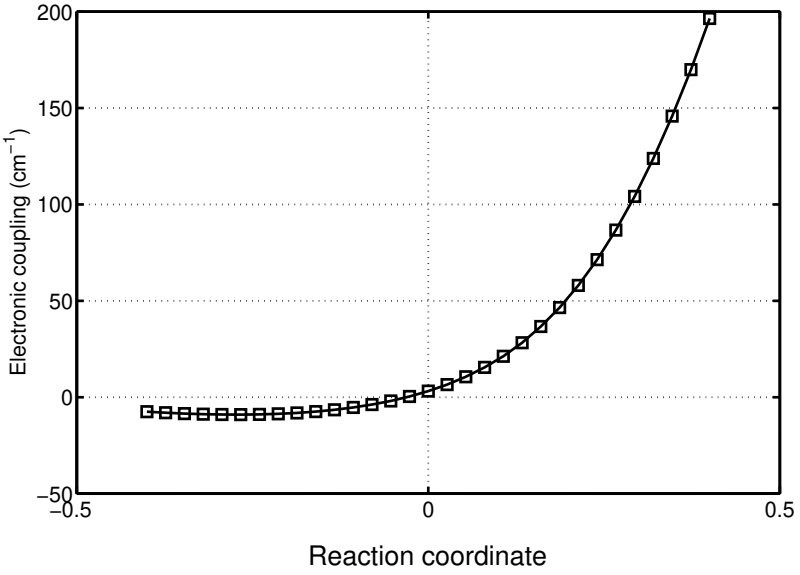

FIG. S7. The fluctuation of electronic coupling modulated by intermolecular rocking mode (177 cm^{-1}).

X. TWO-STATE TWO-MODE MODEL

To illustrate the role of the intermolecular rocking mode, we construct the standard two-state two-mode model based on the parameters from quantum chemistry calculations. In order to simplify the calculation, we only select one high-frequency (tuning) mode which is the intermolecular rocking mode at 177 cm^{-1} in order to construct the PESs. Thus, on the basis of these two modes, a minimal model of a conical intersection can be constructed with the proper parameters.

The total Hamiltonian can be written as

$$\begin{aligned} H &= H_{\mathrm{mol}} + H_{\mathrm{env}}, \\ H_{\mathrm{mol}} &= H_e + H_{TT}, \\ H_e &= |e\rangle \left(h_1 - \epsilon/2\right) \langle e| \,, \\ H_{TT} &= |TT\rangle \left(h_2 + \epsilon/2\right) \langle TT| + \left(|TT\rangle V \langle e| + h.c.\right). \end{aligned} \tag{S5}$$

Here, ϵ is the electronic energy difference between singlet excited state S_1 and triplet-pair state T_1T_1. The vibrational part of the Hamiltonians h_1 and h_2 are associated with the S_1 and T_1T_1 state, respectively. They include two vibrational modes, the tuning (Q_t) and coupling mode (Q_c). They are given by $h_g = \frac{1}{2}\sum_{i=c/t} \Omega_i (P_i^2 + Q_i^2)$ and $h_1 = h_g - \kappa Q_t$ and $h_2 = h_g + \kappa Q_t$, where $\Omega_{i=c/t}$ denotes the vibrational frequencies of the tuning and coupling modes, respectively. In addition, κ is the vibronic coupling strength. The electronic coupling between two electronic excited states is assumed to be linearly related to the coupling mode Q_c, such that $V = \Lambda Q_c$ with the electronic coupling strength Λ. Furthermore, we assume that all relevant interactions between the two electronic PESs are captured by the coupling mode, which is explicitly included. Thus, the bath only couples vibrational states within the same electronic PES, and we assume that the two vibrational modes are coupled to their own linear bath according to the Hamiltonian

$$H_{\mathrm{env}} = \sum_{\alpha} \left[\frac{p_\alpha^2}{2m_\alpha} + \frac{m_\alpha \omega_\alpha^2}{2} \left(x_\alpha + \frac{c_\alpha Q_1}{m_\alpha \omega_\alpha^2} \right)^2 + \frac{q_\alpha^2}{2M_\alpha} + \frac{M_\alpha \nu_\alpha^2}{2} \left(y_\alpha + \frac{d_\alpha Q_2}{M_\alpha \nu_\alpha^2} \right)^2 \right]. \tag{S6}$$

Here, the momenta of the bath oscillators are denoted as p_α and q_α, while their coordinates, masses, and frequencies are denoted by x_α, m_α, ω_α and y_α, M_α, ν_α. The respective coupling constants are c_α and d_α. The baths are

characterized by the spectral densities. Throughout this work, we assume that both the tuning and coupling mode experience fluctuations with an Ohmic spectral distribution according to $J_{c/t}(\omega) = \eta_{c/t}\omega e^{-\omega/\omega_c}$. Here, $\eta_{c/t}$ are the damping strengths for the coupling and tuning mode, respectively, and ω_c is the cutoff frequency. We assume that the two baths have the same cutoff frequencies.

Based on the results for the parameters obtained from the quantum chemistry calculations, we assume for the tuning and coupling modes $\Omega_t = 1013$ cm^{-1} and $\Omega_c = 177$ cm^{-1}, respectively. Moreover, the values of the vibronic coupling strength of the tuning and the coupling modes are obtained from the Huang-Rhys factors and we have $\kappa = 300$ cm^{-1} and $\Lambda = 150$ cm^{-1}. In addition, to mimic the dissipation induced by the phonons in the environment, we assume the damping strength $\eta_c = \eta_t = \eta = 2.0$ and the cutoff frequency $\omega_c = 200$ cm^{-1}. With these parameters, the population dynamics of the wave-packet along the coupling mode has been calculated up to 1 ps. The dynamics along coupling and tuning modes are shown in main text. It clearly shows the wave-packet transfer from the upper state to the lower state within an ultrafast timescale. To quantify the time scale of the population transfer, the wave packet has been summed along the reaction coordinates and the obtained kinetics are shown in Fig. S8. Based on the exponential fitting, we find the transfer time of 180 fs, which is actually slightly larger than the experimental observation of 100 fs. However, this simple two-state two-mode model solely takes into account one high-frequency vibrational mode with strong vibronic coupling. In our measurements, more vibrations are retrieved with strong vibronic couplings, which further reduce the barrier between the singlet excited state and the triplet-pair states. They speed up the transition of the wave packet through the conical intersection. In addition, we show the population transfer at $Q_c = 0$ from S_1 to T_1T_1 in Fig. S9. We observe clear oscillations of the population of the electronic state T_1T_1 with a period of 32 fs, which indicates the vibrational coherence of the tuning mode. Based on our calculation, we demonstrate that the vibrational coherence of the couling mode can not be transferred through the conical intersection, but is determined by the target PES.

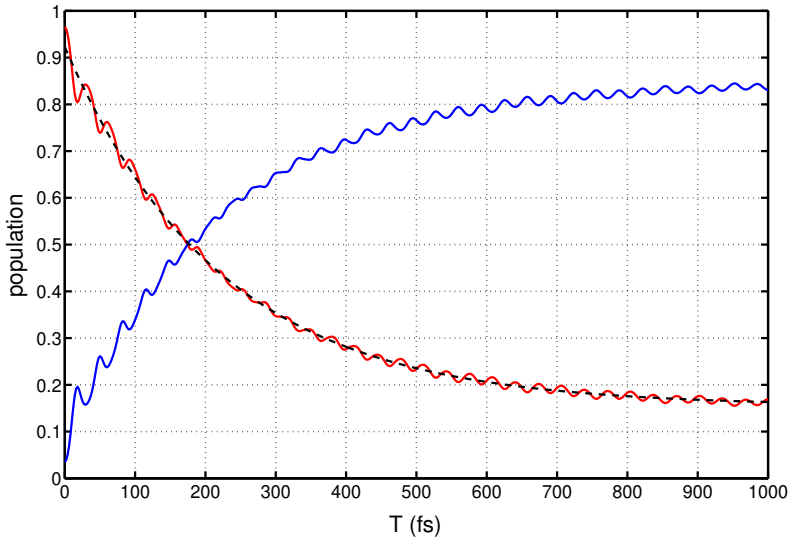

FIG. S8. Population transfer of the wave packet from the higher excited state (red solid line) to the lower excited state (blue solid line) with a time scale of 180 fs.

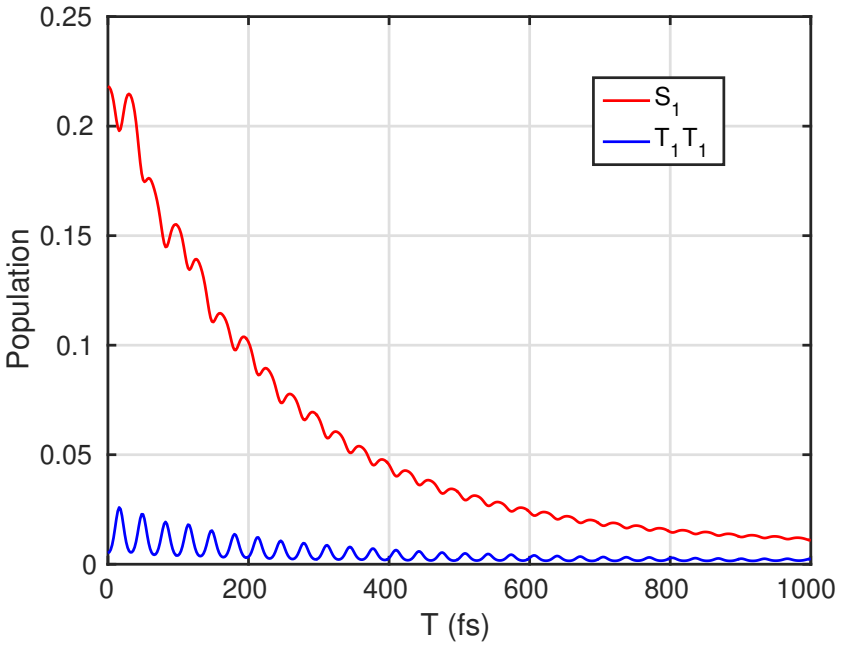

FIG. S9. Population dynamics of the wave packet at $Q_c = 0$ from S_1 to T_1T_1.

REFERENCES AND NOTES

1. M. B. Smith, J. Michl, Singlet fission. *Chem. Rev.* **110**, 6891–6936 (2010).

2. M. J. Y. Tayebjee, D. R. McCamey, T. W. Schmidt, Beyond shockley-queisser: Molecular approaches to high-efficiency photovoltaics. *J. Phys. Chem. Lett.* **6**, 2367–2378 (2015).

3. N. R. Monahan, D. Sun, H. Tamura, K. W. Williams, B. Xu, Y. Zhong, B. Kumar, C. Nuckolls, A. R. Harutyunyan, G. Chen, H.-L. Dai, D. Beljonne, Y. Rao, X.-Y. Zhu, Dynamics of the triplet-pair state reveals the likely coexistence of coherent and incoherent singlet fission in crystalline hexacene. *Nat. Chem.* **9**, 341–346 (2017).

4. M. B. Smith, J. Michl, Recent advances in singlet fission. *Annu. Rev. Phys. Chem.* **64**, 361–386 (2013).

5. A. J. Musser, M. Maiuri, D. Brida, G. Cerullo, R. H. Friend, J. Clark, The nature of singlet exciton fission in carotenoid aggregates. *J. Am. Chem. Soc.* **137**, 5130–5139 (2015).

6. E. A. Margulies, C. E. Miller, Y. Wu, L. Ma, G. C. Schatz, R. M. Young, M. R. Wasielewski, Enabling singlet fission by controlling intramolecular charge transfer in π-stacked covalent terrylenediimide dimers. *Nat. Chem.* **8**, 1120–1125 (2016).

7. E. A. Margulies, J. L. Logsdon, C. E. Miller, L. Ma, E. Simonoff, R. M. Young, G. C. Schatz, M. R. Wasielewski, Direct observation of a charge-transfer state preceding high-yield singlet fission in Terrylenediimide thin films. *J. Am. Chem. Soc.* **139**, 663–671 (2017).

8. K. Miyata, F. S. Conrad-Burton, F. L. Geyer, X.-Y. Zhu, Triplet pair states in singlet fission. *Chem. Rev.* **119**, 4261–4292 (2019).

9. I. Breen, R. Tempelaar, L. A. Bizimana, B. Kloss, D. R. Reichman, D. B. Turner, Triplet separation drives singlet fission after femtosecond correlated triplet pair production in rubrene. *J. Am. Chem. Soc.* **139**, 11745–11751 (2017).

10. R. D. Pensack, E. E. Ostroumov, A. J. Tilley, S. Mazza, C. Grieco, K. J. Thorley, J. B. Asbury, D. S. Seferos, J. E. Anthony, G. D. Scholes, Observation of two triplet-pair intermediates in singlet exciton fission. *J. Phys. Chem. Lett.* **7**, 2370–2375 (2016).

11. D. N. Congreve, J. Lee, N. J. Thompson, E. Hontz, S. R. Yost, P. D. Reusswig, M. E. Bahlke, S. Reineke, T. V. Voorhis, M. A. Baldo, External quantum efficiency above 100% in a singlet-exciton-fissionbased organic photovoltaic cell. *Science* **340**, 334–337 (2013).

12. N. J. Thompson, D. N. Congreve, D. Goldberg, V. M. Menon, M. A. Baldo, Slow light enhanced singlet exciton fission solar cells with a 126% yield of electrons per photon. *Appl. Phys. Lett.* **103**, 263302 (2013).

13. M. W. B. Wilson, A. Rao, B. Ehrler, R. H. Friend, Singlet exciton fission in polycrystalline pentacene: From photophysics toward devices. *Acc. Chem. Res.* **46**, 1330–1338 (2013).

14. C. Jundt, G. Klein, B. Sipp, J. Le Moigne, M. Joucla, A. A. Villaeys, Exciton dynamics in pentacene thin films studied by pump-probe spectroscopy. *Chem. Phys. Lett.* **241**, 84–88 (1995).

15. B. D. Folie, J. B. Haber, S. Refaely-Abramson, J. B. Neaton, N. S. Ginsberg, Long-lived correlated triplet pairs in a π-stacked crystalline pentacene derivative. *J. Am. Chem. Soc.* **140**, 2326–2335 (2018).

16. W.-L. Chan, M. Ligges, X.-Y. Zhu, The energy barrier in singlet fission can be overcome through coherent coupling and entropic gain. *Nat. Chem.* **4**, 840–845 (2012).

17. T. C. Berkelbach, M. S. Hybertsen, D. R. Reichman, Microscopic theory of singlet exciton fission. I. General formulation. *J. Chem. Phys.* **138**, 114102 (2013).

18. T. C. Berkelbach, M. S. Hybertsen, D. R. Reichman, Microscopic theory of singlet exciton fission. II. Application to pentacene dimers and the role of superexchange. *J. Chem. Phys.* **138**, 114103 (2013).

19. T. C. Berkelbach, M. S. Hybertsen, D. R. Reichman, Microscopic theory of singlet exciton fission. III. Crystalline pentacene. *J. Chem. Phys.* **141**, 074705 (2014).

20. T. Zeng, R. Hoffmann, N. Ananth, The low-lying electronic states of pentacene and their roles in singlet fission. *J. Am. Chem. Soc.* **136**, 5755–5764 (2014).

21. H. Tamura, M. Huix-Rotllant, I. Burghardt, Y. Olivier, D. Beljonne, First-principles quantum dynamics of singlet fission: Coherent versus thermally activated mechanisms governed by molecular π stacking. *Phys. Rev. Lett.* **115**, 107401 (2015).

22. J. Zirzlmeier, D. Lehnherr, P. B. Coto, E. T. Chernick, R. Casillas, B. S. Basel, M. Thoss, R. R. Tykwinski, D. M. Guldi, Singlet fission in pentacene dimers. *Proc. Natl. Acad. Sci. U.S.A.* **112**, 5325–5330 (2015).

23. S. N. Sanders, E. Kumarasamy, A. B. Pun, M. T. Trinh, B. Choi, J. Xia, E. J. Taffet, J. Z. Low, J. R. Miller, X. Roy, X.-Y. Zhu, M. L. Steigerwald, M. Y. Sfeir, L. M. Campos, Quantitative intramolecular singlet fission in bipentacenes. *J. Am. Chem. Soc.* **137**, 8965–8972 (2015).

24. S. Lukman, K. Chen, J. M. Hodgkiss, D. H. P. Turban, N. D. M. Hine, S. Dong, J. Wu, N. C. Greenham, A. J. Musser, Tuning the role of charge-transfer states in intramolecular singlet exciton fission through side-group engineering. *Nat. Commun.* **7**, 13622 (2016).

25. S. M. Hart, W. R. Silva, R. R. Frontiera, Femtosecond stimulated Raman evidence for charge-transfer character in pentacene singlet fission. *Chem. Sci.* **9**, 1242–1250 (2018).

26. A. J. Musser, M. Liebel, C. Schnedermann, T. Wende, T. B. Kehoe, A. Rao, P. Kukura, Evidence for conical intersection dynamics mediating ultrafast singlet exciton fission. *Nat. Phys.* **11**, 352–357 (2015).

27. A. A. Bakulin, S. E. Morgan, T. B. Kehoe, M. W. B. Wilson, A. W. Chin, D. Zigmantas, D. Egorova, A. Rao, Real-time observation of multiexcitonic states in ultrafast singlet fission using coherent 2D electronic spectroscopy. *Nat. Chem.* **8**, 16–23 (2016).

28. S. Refaely-Abramson, F. H. da Jornada, S. G. Louie, J. B. Neaton, Origins of singlet fission in solid pentacene from an *ab initio* Green's function approach. *Phys. Rev. Lett.* **119**, 267401 (2017).

29. H. L. Stern, A. Cheminal, S. R. Yost, K. Broch, S. L. Bayliss, K. Chen, M. Tabachnyk, K. Thorley, N. Greenham, J. M. Hodgkiss, J. Anthony, M. Head-Gordon, A. J. Musser, A. Rao, R. H. Friend, Vibronically coherent ultrafast triplet-pair formation and subsequent thermally activated dissociation control efficient endothermic singlet fission. *Nat. Chem.* **9**, 1205–1212 (2017).

30. K. Miyata, Y. Kurashige, K. Watanabe, T. Sugimoto, S. Takahashi, S. Tanaka, J. Takeya, T. Yanai, Y. Matsumoto, Coherent singlet fission activated by symmetry breaking. *Nat. Chem.* **9**, 983–989 (2017).

31. P. J. M. Johnson, A. Halpin, T. Morizumi, V. I. Prokhorenko, O. P. Ernst, R. J. D. Miller, Local vibrational coherences drive the primary photochemistry of vision. *Nat. Chem.* **7**, 980–986 (2015).

32. D. M. Jonas, Vibrational and nonadiabatic coherence in 2D electronic spectroscopy, the Jahn-Teller effect, and energy transfer. *Annu. Rev. Phys. Chem.* **69**, 327–352 (2018).

33. A. Jha, H.-G. Duan, V. Tiwari, P. K. Nayak, H. J. Snaith, M. Thorwart, R. J. D. Miller, Direct observation of ultrafast exciton dissociation in lead iodide perovskite by 2D electronic spectroscopy. *ACS Photonics*, **5**, 852–860 (2018).

34. A. Rao, M. W. B. Wilson, S. Albert-Seifried, R. D. Pietro, R. H. Friend, Photophysics of pentacene thin flim: The role of exciton fission and heating effects. *Phys. Rev. B* **84**, 195411 (2011).

35. V. Butkus, D. Zigmantas, L. Valkunas, D. Abramavicius, Vibrational vs. electronic coherence in 2D spectrum of molecular systems. *Chem. Phys. Lett.* **545**, 40–43 (2012).

36. R. Xian, G. Corthey, D. M. Rogers, C. A. Morrison, V. I. Prokhorenko, S. A. Hayes, R. J. Dwayne Miller, Coherent ultrafast lattice-directed reaction dynamics of triiodide anion photodissociation. *Nat. Chem.* **9**, 516–522 (2017).

37. S. Schiefer, M. Huth, A. Dobrinevski, B. Nickel, Determination of the crystal structure of substrate-induced pentacene polymorphs in fiber structured thin films. *J. Am. Chem. Soc.* **129**, 10316–10317 (2007).

38. S. Ito, T. Nagami, M. Nakano, Density analysis of intra- and intermolecular vibronic couplings toward bath engineering for singlet fission. *J. Phys. Chem. Lett.* **6**, 4972–4977 (2015).

39. Ab initio exciton model calculations show rather weak electronic couplings between the singlet exciton and the triplet-pair state, $V = 6\ \mathrm{cm}^{-1}$ due to the quite different electronic configuration of the singlet and triplet-pair states. This value is smaller than the parameters used in (*27*).

40. A. Ishizaki, Y. Tanimura, Quantum dynamics of system strongly coupled to low-temperature colored noise bath: Reduced hierarchy equations approach. *J. Phys. Soc. Jpn.* **74**, 3131–3134 (2005).

41. C. Kreisbeck, T. Kramer, Long-lived electronic coherence in dissipative exciton dynamics of light-harvesting complexes. *J. Phys. Chem. Lett.* **3**, 2828–2833 (2012).

42. M. Tsuchimoto, Y. Tanimura, Spins dynamics in a dissipative environment: Hierarchal equations of motion approach using a graphics processing unit (GPU). *J. Chem. Theory Comput.* **11**, 3859–3865 (2015).

43. Based on our two-state two-mode model, the transfer with time ∼180 fs of the PSF is slightly slower than the observation of ∼100 fs. With few high-frequency modes, we expect that a multichannel modeling of a conical intersection speeds up the population transfer. However, the computational costs of the simulations are too large with the numerically exact method.

44. H.-G. Duan, V. I. Prokhorenko, R. J. Cogdell, K. Ashraf, A. L. Stevens, M. Thorwart, R. J. D. Miller, Nature does not rely on long-lived electronic quantum coherence for photosynthetic energy transfer. *Proc. Natl. Acad. Sci. U.S.A.* **114**, 8493–8498 (2017).

45. A. Halpin, P. J. M. Johnson, R. Tempelaar, R. S. Murphy, J. Knoester, T. L. C. Jansen, R. J. D. Miller, Two-dimensional spectroscopy of a molecular dimer unveils the effects of vibronic coupling on exciton coherences. *Nat. Chem.* **6**, 196–201 (2014).

46. H.-G. Duan, P. Nalbach, R. J. D. Miller, M. Thorwart, Ultrafast energy transfer in excitonically-coupled molecules induced by a nonlocal Peierls phonon. *J. Phys. Chem. Lett.* **10**, 1206–1211 (2019).

47. V. I. Prokhorenko, A. Picchiotti, S. Maneshi, R. J. D. Miller, Broadband electronic two-dimensional spectroscopy in the deep UV. *Ultrafast Phenomena XIX* **162**, 432–435 (2015).

48. J. D. Hybl, A. A. Ferro, D. M. Jonas, Two-dimensional fourier transform electronic spectroscopy. *J. Chem. Phys.* **115**, 6606 (2001).

49. X. Li, R. M. Parrish, F. Liu, S. I. L. Kokkila Schumacher, T. J. Martínez, An ab initio exciton model including charge-transfer excited states. *J. Chem. Theo. Comput.* **13**, 3493–3504 (2017).

50. J. Wang, R. M. Wolf, J. W. Caldwell, P. A. Kollman, D. A. Case, Development and testing of a general amber force field. *J. Comput. Chem.* **15**, 1157–1174 (2004).

51. M. A. Rohrdanz, K. M. Martins, J. M. Herbert, A long-range-corrected density functional that performs well for both ground-state properties and time-dependent density functional theory excitation energies, including charge-transfer excited states. *J. Chem. Phys.* **130**, 054112 (2009).

52. T. H. Dunning Jr., Gaussian basis sets for use in correlated molecular calculations. I. The atoms boron through neon and hydrogen. *J. Chem. Phys.* **90**, 1007–1023 (1989).

53. S. Grimme, J. Antony, S. Ehrlich, H. Krieg, A consistent and accurate *ab initio* parametrization of density functional dispersion correction (DFT-D) for the 94 elements H-Pu. *J. Chem. Phys.* **132**, 154104 (2010).

54. S. Grimme, S. Ehrlich, L. Goerigk, Effect of the damping function in dispersion corrected density functional theory. *J. Comput. Chem.* **32**, 1456–1465 (2011).

55. I. S. Ufimtsev, T. J. Martinez, Quantum chemistry on graphical processing units. 2. Direct self-consistent-field implementation. *J. Chem. Theory Comput.* **5**, 1004–1015 (2009).

56. A. Sisto, D. R. Glowacki, T. J. Martinez, Ab initio nonadiabatic dynamics of multichromophore complexes: A scalable graphical-processing-unit-accelerated exciton framework. *Acc. Chem. Res.* **47**, 2857–2866 (2014).

57. U. Manthe, H. Köppel, New method for calculating wave packet dynamics: Strongly coupled surfaces and the adiabatic basis. *J. Chem. Phys.* **93**, 345 (1990).

58. D.-L. Qi, H.-G. Duan, Z.-R. Sun, R. J. D. Miller, M. Thorwart, Tracking an electronic wave packet in the vicinity of a conical intersection. *J. Chem. Phys.* **147**, 074101 (2017).

59. V. I. Prokhorenko, Global analysis of multi-dimensional experimental data. *European Photochemistry Association Newletter* June 2012, p. 21.

60. F. Milota, V. I. Prokhorenko, T. Mancal, H. von Berlepsch, O. Bixner, H. F. Kauffmann, J. Hauer, Vibronic and vibrational coherences in two-dimensional electronic spectra of supramolecular J-Aggregates. *J. Phys. Chem. A* **117**, 6007–6014 (2013).

61. A. Cohen, J. Kovačevič, Wavelets: The mathematical background. *Proc. IEEE* **84**, 514–522 (1996).

62. J. D. Harrop, S. N. Taraskin, S. R. Elliot, Instantaneous frequency and amplitude identification using wavelets: Application to glass structure. *Phys. Rev. E Stat. Nonlin. Soft Matter. Phys.* **66**, 026703 (2002).

63. J. van den Berg, *Wavelets in Physics* (Cambridge Univ. Press, 2004).